

Ashok Kumar Nallathambi,<sup>1</sup> Yalcin Kaymak,<sup>1</sup> Eckehard Specht,<sup>1</sup> and Albrecht Bertram<sup>1</sup>

## Optimum Strategies to Reduce Residual Stresses and Distortion during the Metal Quenching Process

**ABSTRACT:** Quenching is a complex thermo-mechano-metallurgical problem. Unexplored or without an optimized cooling strategy, a quenching process can end up with high residual stresses and distortion. This paper presents the mathematical formulation of the physics behind the quenching process, the numerical technique and optimization of the cooling strategies for the selected geometries. The finite element method (FEM) is used to solve the coupled partial differential equations in the framework of an isothermal-staggered approach. The solid-solid phase transformations are modeled using a linear iso-kinetic law with Schiel's additivity rule and Koistinen-Marburger (KM) law. The thermoplastic material model is formulated on the basis of  $J_2$ -plasticity theory with a temperature and phase fraction-dependent yield limit together with the appropriate mixture rule. The coupling effects such as phase transformation enthalpy, transformation-induced plasticity and dissipation are considered. The local heat transfer coefficient (HTC) during the quenching process plays a crucial role for the evolution of the distortion and residual stresses. It is demonstrated that with an enhanced quenching at the mass lumped regions, the distortion can be reduced. It is always possible to find an HTC profile which eliminates the distortion completely on the expense of an increased residual stress state. Therefore, an optimum quenching strategy has to be found to reduce the distortion and the residual stresses simultaneously. It is shown that with an enhanced quenching at the mass lumped regions and with a reduced quenching at the edges and corners, stresses and distortion can be minimized simultaneously. Examples are given for different kinds of metals and geometries such as long profiles (L and T) and disk with a hole.

**KEYWORDS:** quenching, residual stress, distortion, FEM, phase transformation, plasticity, optimization

### Introduction

Most of the metallic parts have to be quenched after the thermal treatment processes to obtain the required properties such as hardness, micro-structure, etc. However, during the quenching process, transient heat conduction, metallic phase transformation, and plastic behavior of the metals introduce high residual stresses and distortion, which worsen the product quality and production efficiency. Although there are methods to correct the distortion such as stretching, secondary plastic bending, etc., they are usually difficult to apply, expensive, and time consuming. Moreover, most of the distortion elimination methods are not applicable to many products such as those requiring polished scratch free surfaces. The residual stresses accompanying the distortion during the quenching process increase the possibilities for the growth of micro-cracks under the action of fatigue loading. Even though a complete elimination of the residual stresses is practically impossible, considerable reduction in both the distortion and residual stresses are highly preferable for an efficient quenching process. In this paper, an attempt is made for the simultaneous reduction of distortion and residual stresses through optimizing the local enhanced and reduced HTCs in relation to the mass concentration in the geometry. Some of the important literatures related to this work are reviewed briefly in this section which also includes the previous works of the authors [1–5].

In a quenching process simulation, three essential physical fields to be coupled are as follows: (i) thermal, (ii) metallurgical, and (iii) displacement field. The heat flow method [6] or heat source method is used for including the latent heat effect in thermal equilibrium equation and the FEM is employed for the numerical solution. Pure metals like aluminum, copper, and nickel are relatively easier to model due to the absence of metallurgical fields. In steel-like alloys, solid-solid phase transformation increases the difficulty of the quenching process modeling. Çetinel et al. [7] simulated and experimentally verified the micro structural evolution of steels subjected to tempcore process (inner austenite tempers the outer martensite)

Manuscript received April 15, 2008; accepted for publication February 19, 2009; published online March 2009.

<sup>1</sup> Otto von Guericke University, Magdeburg 39106, Germany, e-mail: [ashok.nallathambi@st.ovgu.de](mailto:ashok.nallathambi@st.ovgu.de)

using FEM. Multiphase evolutions in steel have been modeled by Reti et al. [8] and Kang and Im [9]. Koistinen-Marburger (KM) model, Yu's law, and Magee's kinetic rule have been widely used for the evolution of martensitic phase. Yu's law [10] includes both the martensite start and finish temperature but do not incorporate the stress dependency of the transformation. The modified versions of KM model [3,9,11,12], include the stress dependency of martensitic transformation but do not consider the martensite end temperature. Recent Magee's kinetic rule [13–16] predicts the martensitic transformation accurately, which requires the experimental determination of several coefficients. Fachinotti et al. [10] presented a detailed discussion of the advantage of using additivity rule instead of using Johnson-Mehl-Avrami-Kolmogorov (JMAK) rate model for deriving continuous cooling transformation (CCT) diagram from the isothermal transformation (IT) diagram in the case of pearlitic evolution.

The shape change during the quenching process occurs due to the elastic, plastic, thermal phase changes and transformation induced plastic strains. The stress tensor can be estimated from the elastic part of the strain tensor using the constitutive law of the material. Elastic model [17], elastic-perfectly plastic [18], elastic-plastic with isotropic [3,11,19], kinematic hardening [19], and combined hardening rule [14] are the frequently used stress-strain relations in the literature. The Voce-mechanical threshold stress constitutive model has been used by Newman et al. [20] for the W319 aluminum, unidirectional beam quenching process.

As an extension of our previous works, a logical optimization technique for the simultaneous reduction of the distortion and residual stresses is introduced for the metal quenching process. The martensitic transformation is modeled using the KM model. The diffusive phase transformation is modeled using the newly introduced linear isokinetic law with Schiel's additivity rule. An isotropic strain hardening material model with a temperature and phase fraction dependent von-Mises yield criterion is employed for the plasticity calculation. A correct combination of enhanced and reduced cooling based on mass distribution of the material, reduces the distortion and residual stresses simultaneously. An appropriate HTC profile is identified for the L and T profiles, and disk with a hole made up of aluminum and 100Cr6 steel. The next section presents the mathematical formulation of the quenching process which includes the thermal, metallurgical, and mechanical fields. The FEM implementation with the isothermal staggered approach based solution methodology is described in the Solution Methodology section. A procedure to find an optimum HTC profile with examples are discussed in the Results and Discussions section. The equal and optimized cooling strategies are compared and the advantages of the optimum strategy are illustrated.

### Mathematical Formulation

During the quenching process, the temperature, micro-structure, and stresses at every material point change with respect to time. The distortion is originated from the nonuniform volume changes occurring due to thermal shrinkage and phase transitions. It is a permanent deformation because of the material yielding and transformation induced plastic flow. The thermal, metallurgical, and mechanical fields are modeled separately and discussed in detail.

#### Thermal Field

Let an open bounded domain  $\Omega \subset \mathbb{R}^{n_d}$  ( $n_d=1,2,3$ ) be the configuration of a nonlinear thermo-plastic body  $B$  with particles defined by  $\vec{X} \in \tilde{\Omega}$ ,  $\Gamma = \partial\Omega$  its smooth boundary and the time interval of analysis  $t \in Y$  ( $Y \subset \mathbb{R}^+$ ). As usual,  $\tilde{\Omega} = \Omega \cup \Gamma$  and  $\Gamma = \Gamma_\theta \cup \Gamma_q$ . The *metal quenching* problem consists of finding the absolute temperature field  $\theta: \tilde{\Omega} \times Y \rightarrow \mathbb{R}^+$  such that [21]

$$\rho c_p \dot{\theta} = -\nabla \cdot \vec{q} + q_v \quad \text{in } \tilde{\Omega} \times Y \quad (1)$$

subject to the boundary conditions

$$\theta = \theta_s \quad \text{in } \Gamma_\theta \times Y \quad (2)$$

$$\vec{q} \cdot \vec{n} + q_s = 0 \quad \text{in } \Gamma_q \times Y \quad (3)$$

and the initial condition

$$\theta(\vec{X}, t)|_{t=0} = \theta_0(\vec{X}) \quad \text{in } \Omega \quad (4)$$

Equation 1 represents the energy balance obtained from the First Law of Thermodynamics. The super-imposed dot denotes time derivative,  $\nabla$  is the gradient operator with respect to Cartesian reference system,  $\rho$  is the density and  $c_p$  is the specific heat capacity, both of which are function of temperature and phase fractions ( $f_j$ ).  $q_v$  is the heat generation per unit volume and  $\vec{q}$  is the heat flux vector. The internal heat generation ( $q_v$ ) accounts both the phase transformation enthalpies and mechanical energy dissipation and given as

$$q_v = \chi \sigma_y \dot{\epsilon}^p + \sum_{j=1}^{n_p} L_j \dot{f}_j \quad (5)$$

where  $\chi$  is the fraction of mechanical energy converted into thermal energy,  $\sigma_y$  is the yield strength,  $\dot{\epsilon}^p$  is the rate of effective plastic strain,  $L_j$  is the latent heat of the individual phase transformation,  $\dot{f}_j$  is the phase transition rate and  $n_p$  is the number of product phases.

In Equation 2,  $\theta_s$  is the prescribed surface temperature on  $\Gamma_\theta$ . On the heat flux boundary  $\Gamma_q$ ,  $q_s$  is the normal heat flux due to convection-radiation phenomenon. Using the temperature-dependent overall heat transfer coefficient (HTC)  $\alpha$ ,  $q_s$  can be stated according to Newton's law of convection as

$$q_s = -\alpha(\theta)(\theta - \theta_\infty) \quad (6)$$

where  $\theta$  is the surface temperature,  $\theta_\infty$  is the ambient temperature. Fourier's law of heat conduction states that heat flux vector  $\vec{q}$  is proportional to the temperature gradient

$$\vec{q} = -\mathbf{k}(\theta, f_j) \cdot \nabla \theta \quad (7)$$

where  $\mathbf{k}$  is the temperature and phase fractions dependent second-order thermal conductivity tensor.

#### Phase Transformation Field

Phase transformations in solids can be classified as: diffusive and displacive transformations. During the transformations in steel, the parent phase austenite may transform into product phases such as pearlite (diffusive) and martensite (displacive). Unlike the diffusive, the displacive transformation is time-independent.

**Diffusive Transformation**—The evolution of the diffusive phase transitions is best described by time-temperature-transformation (TTT) diagrams, which are constructed using the isothermal phase change data. The IT (also named TTT) diagrams can be obtained from the JMAK law [9]. In the IT diagram, the double C-curves are plotted for 1 % (the transformation start time,  $t_s$ ) and 99 % (the transformation end time,  $t_e$ ) of the product phase fraction at every temperature  $\theta$  using the JMAK law. The isothermal formation of the new phase is described in this work by a simple linear isokinetic rule [5],

$$\dot{f} = \frac{1}{t_e - t_s} \quad (8)$$

which states that the rate of phase transformation is constant in isothermal case. The transformation start time  $t_s$  and end time  $t_e$  are obtained from the IT diagram. In the nonisothermal case, the cooling curve is considered to be composed of small isothermal steps. The transformation begins at the incubation time  $t_{inc}$  and it ends when the phase fraction reaches unity or the temperature is out of the transformation range. Using Scheil's additivity rule, the incubation time is given as

$$\int_0^{t_{inc}} \frac{1}{t_s(\theta(t))} dt = 1 \quad (9)$$

**Displacive Transformation**—Shear-dominant, diffusionless, martensitic transformations occur when the temperature of the steel drops below a critical temperature  $M_s$  rapidly. Martensite, which is hard and brittle, is a solid solution of carbon in tetragonally distorted BCC iron. In this work, the displacive transformation is modeled using the KM law [5]

$$f_M = f_A \{1 - \exp[k_M(\theta - M_s)]\}, \quad \text{when } \theta < M_s \quad (10)$$

where  $f_M$  and  $f_A$  are martensite and austenite phase fractions,  $M_s$  is the martensite start temperature and  $k_M$  ( $\approx 0.011$ ) is the stress dependent transformation constant.

### Displacement Field

A thermo-plastic continuum body  $\mathcal{B}$  with interior  $\Omega \subset \mathbb{R}^{n_d}$  ( $n_d=1,2,3$ ) and displacement boundary  $\Gamma_u$ , traction boundary  $\Gamma_t$ ,  $\Gamma = \Gamma_u \cup \Gamma_t$ , together as mentioned in thermal field as  $\tilde{\Omega} = \Omega \cup \Gamma$  and the time interval of analysis  $t \in Y$  ( $Y \subset \mathbb{R}^+$ ), has to satisfy the equilibrium equation at the current spatial configuration  $\vec{x} \in \tilde{\Omega}$ . The equilibrium equation which yields the displacement solution  $\vec{u}$  is given as in Ref [22]

$$\nabla \cdot \mathbf{T} + \vec{b} = \vec{0} \quad \text{in } \tilde{\Omega} \times Y \quad (11)$$

subject to the boundary conditions

$$\vec{u} = \vec{u}_s \quad \text{in } \Gamma_u \times Y \quad (12)$$

$$\mathbf{T} \cdot \vec{n} = \vec{t} \quad \text{in } \Gamma_t \times Y \quad (13)$$

where  $\mathbf{T}$  is the stress tensor,  $\vec{b}$  is the body force vector,  $\vec{u}_s$  is the prescribed displacement vector and  $\vec{t}$  is the prescribed traction vector with unit outward normal  $\vec{n}$ .

The total deformation observed in the quenching process is less than 4 %. Therefore, using the advantage of small deformation theory, the total strain  $\mathbf{E}$  can be additively decomposed into four components as [3]

$$\mathbf{E} = \frac{1}{2} [\nabla \vec{u} + (\nabla \vec{u})^T] = \mathbf{E}^e + \mathbf{E}^p + \mathbf{E}^{tp} + \mathbf{E}^{trip} \quad (14)$$

where  $\mathbf{E}^e$  is the elastic strain tensor,  $\mathbf{E}^p$  is the plastic part of strain tensor,  $\mathbf{E}^{trip}$  is the Transformation Induced Plastic (TRIP) strain tensor, and  $\mathbf{E}^{tp}$  is the volumetric strain tensor due to temperature and phase changes. Once estimating the plastic, the thermal phase change, and the TRIP strain tensors, the elastic strain tensor can be obtained from the total strain tensor, and its methods of estimation are discussed in the subsequent subsections in detail. Using the elastic part of the strain tensor  $\mathbf{E}^e$ , stress tensor  $\mathbf{T}$  can be determined from the constitutive law of the material.

**Volumetric Thermal Phase Change Strain**—During the quenching process, the temperature and phase fractions of the material change continuously. The density of the phase-changing material is a function of temperature and phase fractions. For nonphase-changing materials like aluminum, copper, nickel, etc., the density depends only on temperature. This nature of varying density produces a reversible strain  $\mathbf{E}^{tp}$ . Instead of using the coefficient of thermal expansion,  $\mathbf{E}^{tp}$  is expressed in terms of reference density  $\rho_R$  and current density  $\rho(\theta, f_i)$  of the mixture

$$\mathbf{E}^{tp} = \left( \sqrt[3]{\frac{\rho_R}{\rho(\theta, f_i)}} - 1 \right) \mathbf{I} \quad (15)$$

**Transformation Induced Plastic (TRIP) Strain**—During the phase change period, austenite may transform into any combination of the following micro-structures: pearlite, bainite, and martensite. There is an irreversible strain always associated with the phase change phenomena which is known as TRIP strain and it is proportional to the stress deviator  $\mathbf{T}'$  and rates of phase transformation  $\dot{f}_i$ . Even though the induced stress lies within the yield limit, the TRIP strain occurs in phase changing materials like steel. The TRIP strain rate can be calculated from the macroscopic material behavior based on the micro-mechanical approach and it is given as in Ref [5]

$$\dot{\mathbf{E}}^{trip} = -\frac{3}{2} \mathbf{T}' \sum_{j=1}^{n_p} \{\Lambda_j \ln(f_j) \dot{f}_j\} \quad (16)$$

where  $\Lambda_i$  is called Greenwood-Johnson (GJ) coefficient [23] which must be determined experimentally. The GJ coefficient expresses the compensation of the volume mismatch which produces a plastification in a phase transformation micro region. An approximation for the factor is given by

$$\Lambda_j = \frac{5(\rho_A - \rho_j)}{6\rho_A \sigma_{yA}} \quad (17)$$

where the subscript  $A$  represents the softer phase (usually austenite), and the subscript  $j$  denotes the stronger phase.

**Plastic Strain**—When the equivalent stress exceeds the yield stress, plastic strain occurs. Using a classical rate-independent, isotropic, thermo-plastic material model with temperature and phase fraction-dependent constitutive law and systematically employing the yield criterion, loading criterion, flow rule, hardening rule and consistency condition which are discussed separately in detail, the plastic strain can be estimated. The isotropic constitutive law of the material can be written as in Ref [22]

$$\mathbf{T} = \mathbf{C}^e : \mathbf{E}^e = \kappa \text{tr}(\mathbf{E} - \mathbf{E}^p) \mathbf{I} + 2\mu(\mathbf{E}' - \mathbf{E}^{trip} - \mathbf{E}^p) \quad (18)$$

where  $\mathbf{C}^e$  is the fourth-order elasticity tensor,  $\kappa$  is the bulk modulus and  $\mu$  is the shear modulus which are functions of temperature and phase fractions.

1. **Yield criterion:** The von-Mises yield criteria has the special feature of the smooth surface with convexity which is more suitable for pressure independent ductile materials and given as

$$\phi(\mathbf{T}', \epsilon^p, \theta, f_j) = \|\mathbf{T}'\| - \sqrt{\frac{2}{3}} \sigma_y(\epsilon^p, \theta, f_j) \quad (19)$$

where  $\epsilon^p$  is the effective plastic strain which is used as a strain hardening internal variable, and  $\sigma_y$  is the temperature and phase fractions dependent yield strength.

2. **Loading criterion:** The loading criterion can be stated as in Ref [24],

$$\phi = 0 \quad \text{and} \quad \dot{\phi}|_{\epsilon^p = \text{const}} > 0 \text{ loading}$$

$$\phi = 0 \quad \text{and} \quad \dot{\phi}|_{\epsilon^p = \text{const}} = 0 \text{ neutral loading}$$

$$\phi = 0 \quad \text{and} \quad \dot{\phi}|_{\epsilon^p = \text{const}} < 0 \text{ unloading}$$

where

$$\dot{\phi} = \frac{\partial \phi}{\partial \mathbf{T}'} : \mathbf{T}' + \frac{\partial \phi}{\partial \theta} \dot{\theta} + \frac{\partial \phi}{\partial \epsilon^p} \dot{\epsilon}^p + \sum_{j=1}^{n_p} \frac{\partial \phi}{\partial f_j} \dot{f}_j$$

3. **Flow rule:** An associated flow rule is employed and given as in Ref [24]

$$\dot{\mathbf{E}}^p = \dot{\lambda} \frac{\partial \phi}{\partial \mathbf{T}} = \dot{\lambda} \frac{\mathbf{T}'}{\|\mathbf{T}'\|} = \dot{\lambda} \mathbf{n}_T' \quad (20)$$

where  $\dot{\lambda}$  and  $\mathbf{n}_T'$  are the plastic multiplier and the flow surface normal or stress deviator direction, respectively.

4. **Hardening rule:** A linear isotropic hardening rule is considered, and the yield strength is stated as in Ref [24]

$$\sigma_y(\epsilon^p, \theta, f_j) = \sigma_{y0}(\theta, f_j) + H(\theta, f_j) \epsilon^p \quad (21)$$

where  $\sigma_{y0}$  is the yield strength at the virgin state, and  $H$  is the plastic modulus. The hardening state variable is integrated from the plastic multiplier

$$\epsilon^p = \sqrt{\frac{2}{3}} \dot{\lambda} \quad (22)$$

5. **Consistency condition:** In general, the consistency condition ( $\dot{\phi}=0$ ) yields the value of plastic multiplier  $\dot{\lambda}$ . The isothermal staggered algorithm [25] suggests that the temperature and phase fractions are kept constant (i.e.,  $\dot{\theta}=0$  and  $\dot{f}_j=0$ ), the computation of the plastic multiplier [22] reduces as

$$\dot{\lambda} = \frac{2\mu \mathbf{n}'_T \cdot (\dot{\mathbf{E}} - \dot{\mathbf{E}}^{trip})}{2\mu + \frac{2}{3}H} \quad (23)$$

The continuum tangential elasto-plastic material operator  $\mathbf{C}^{ep}$  for fixed temperature and phase fractions can be given as

$$\mathbf{C}^{ep} = \frac{\partial \mathbf{T}}{\partial \dot{\mathbf{E}}^{ep}} = \mathbf{C}^e - \frac{2\mu}{1 + \frac{H}{3\mu}} \mathbf{n}'_T \otimes \mathbf{n}'_T = 3\kappa \underbrace{\left( \frac{1}{3} \mathbf{I} \otimes \mathbf{I} \right)}_{\mathbf{P}_1} + 2\mu \underbrace{\left( \mathbf{I} - \frac{1}{3} \mathbf{I} \otimes \mathbf{I} \right)}_{\mathbf{P}_2} - \frac{2\mu}{1 + \frac{H}{3\mu}} \mathbf{n}'_T \otimes \mathbf{n}'_T \quad (24)$$

where  $\mathbf{I}$ ,  $\mathbf{P}_1$ , and  $\mathbf{P}_2$  are the fourth-order identity tensor, the spherical, and the deviatoric projectors, respectively.

### Solution Methodology

The FEM is implemented for the solution of the thermal and mechanical equilibrium equations. Nonlinear coupled simultaneous equations obtained through FEM are solved using isothermal staggered algorithm [25,26]. Thermal, metallurgical, and mechanical fields are solved sequentially in every time step in the following way:

1. The thermal field is solved at a fixed configuration and phase fractions.
2. The metallurgical field is solved at a fixed configuration and constant temperature.
3. The mechanical field is solved at a constant temperature and phase fractions.

In each time step, first the transient temperature field is solved iteratively, then the phase transitions are computed, and finally the displacement field is computed iteratively using full Newton-Raphson method. The discrete form of all coupled equations are derived and discussed in detail in the following subsections.

#### Thermal Field Formulation

For an arbitrarily chosen temperature distribution  $\tilde{\theta}$ , the thermal equilibrium condition in Eq 1 has to satisfy the following integral based on virtual temperature principle as

$$\int_{\Omega} [\nabla \cdot (\mathbf{k} \cdot \nabla \theta) + q_v - \rho c_p \dot{\theta}] \tilde{\theta} d\Omega = 0 \quad (25)$$

For an isotropic material, the thermal conductivity tensor  $\mathbf{k}$  can be reduced to a scalar  $k$  which is known as thermal conductivity. Applying Gauss divergence theorem on natural thermal boundary condition Eq 3 and substituting Eq 6 in Eq 25 and it becomes

$$\int_{\Omega} [\nabla \tilde{\theta} \cdot (k \nabla \theta)] d\Omega + \int_{\Omega} [\tilde{\theta} \rho c_p \dot{\theta}] d\Omega + \int_{\Gamma_q} [\tilde{\theta} h \theta] d\Gamma_q = \int_{\Omega} [\tilde{\theta} q_v] d\Omega + \int_{\Gamma_q} [\tilde{\theta} h \theta_{\infty}] d\Gamma_q \quad (26)$$

Using standard isoparametric element interpolation technique, element temperature  $\theta_e$  and its spatial gradients are given as

$$\theta_e = \mathbf{N}^T \boldsymbol{\Theta}_e$$

$$\nabla \theta_e = \nabla \mathbf{N}^T \boldsymbol{\Theta}_e = \mathbf{H} \boldsymbol{\Theta}_e \quad (27)$$

where  $\mathbf{N}$  is the element shape function,  $\boldsymbol{\Theta}_e = \{\theta_1 \ \theta_2 \dots \theta_{\beta}\}^T$  is the element nodal temperature vector,  $\beta$  is the number of nodes per element in the thermal problem, and  $\mathbf{H}$  is the element temperature-gradient interpo-

lation operator. Substituting Eq 27 in Eq 26,  $\tilde{\Theta}_e$  can be eliminated from both sides. Using the implicit Euler backward time difference scheme, the nodal temperature vector and its time derivatives for the current iteration ( $i+1$ ) and current time step ( $t+\Delta t$ ) are given as

$$\begin{aligned}\Theta_{i+1}^{t+\Delta t} &= \Theta_i^{t+\Delta t} + \Delta\Theta \\ \dot{\Theta}_{i+1}^{t+\Delta t} &= \frac{\Theta_i^{t+\Delta t} + \Delta\Theta - \Theta^t}{\Delta t}\end{aligned}\quad (28)$$

Utilizing Eq 28 in the previous equation, the final matrix form of thermal equilibrium is given as

$$\left\{ \mathbf{K}_i^{\theta^{t+\Delta t}} + \frac{1}{\Delta t} \mathbf{C}_i^{\theta^{t+\Delta t}} \right\} (\Delta\Theta) = \mathbf{F}^{\theta^{t+\Delta t}} - \mathbf{R}_i^{\theta^{t+\Delta t}} \quad (29)$$

where  $\mathbf{K}^\theta$  is the global conductance matrix,  $\mathbf{C}^\theta$  is the global capacitance matrix,  $\mathbf{F}^\theta$  is the global thermal force vector, and  $\mathbf{R}^\theta$  is the global residual thermal force vector. The elemental form of these matrices and vectors are given as in Ref [27]

$$\begin{aligned}\mathbf{K}_{e_i}^{\theta^{t+\Delta t}} &= \int_{\Omega} [\mathbf{H}^T k_i^{t+\Delta t} \mathbf{H}] d\Omega + \int_{\Gamma_q} [\mathbf{N}^S h_i^{t+\Delta t} (\mathbf{N}^S)^T] d\Gamma_q \\ \mathbf{C}_{e_i}^{\theta^{t+\Delta t}} &= \int_{\Omega} [\mathbf{N} \rho_i^{t+\Delta t} c_{p_i}^{t+\Delta t} \mathbf{N}^T] d\Omega \\ \mathbf{F}_i^{\theta^{t+\Delta t}} &= \int_{\Omega} [\mathbf{N} q_{v_i}^{t+\Delta t}] d\Omega + \int_{\Gamma_q} [\mathbf{N} h_i^{t+\Delta t} \theta_{\infty}] d\Gamma_q \\ \mathbf{R}_{e_i}^{\theta^{t+\Delta t}} &= \left\{ \int_{\Omega} [\mathbf{H}^T k_i^{t+\Delta t} \mathbf{H}] d\Omega \right\} \Theta_{e_i}^{t+\Delta t} + \mathbf{C}_{e_i}^{\theta^{t+\Delta t}} \left( \frac{\Theta_{e_i}^{t+\Delta t} - \Theta_e^t}{\Delta t} \right)\end{aligned}\quad (30)$$

### Phase Field Formulation

At the end of thermal field computation, the current temperature  $\theta^{t+\Delta t}$  and current temperature increment  $\Delta\theta = \theta^{t+\Delta t} - \theta^t$  are known at every integration point of the elements. The displacive and diffusive phase transitions are computed using these temperature details.

*Diffusive Phase Transitions*—In this work, pearlite is considered as the only product of diffusive transformation which is a reasonable simplification. Scheil's sum increment  $\Delta S$  at the current time step can be computed using the IT diagram informations and given as in Ref [5]

$$\Delta S = \frac{\Delta t}{t_s^{t+0.5\Delta t}} \quad (31)$$

The current Scheil's sum can be updated to  $S^{t+\Delta t} = S^t + \Delta S$ . The general phase fraction evolved during the current time step can be given as

$$\Delta f = \frac{\zeta \Delta t}{t_e^{t+0.5\Delta t} - t_s^{t+0.5\Delta t}} \quad (32)$$

The following three possibilities arise in this calculation:

- If  $S^{t+\Delta t} < 1$ , then  $\Delta f = 0$ .
- If  $S^t < 1$  and  $S^{t+\Delta t} < 1$ , the incubation time is reached during the current time step, and only a fraction  $\zeta$  of  $\Delta t$  contributes to phase transition and  $\zeta \approx (S^{t+\Delta t} - 1) / \Delta S$ .
- If  $S^{t+\Delta t} > 1$  and also  $S^t > 1$ , the phase transition already started and  $\zeta = 1$ , since the full time step contributes to phase transition.

*Displacive Phase Transitions*—The stress dependency of the martensitic transformation coefficient  $k_M$  in Eq 10 can be included in the model by introducing additional stress coefficients given as

$$f_M^{t+\Delta t} = f_A^{t+\Delta t} \{1 - \exp[k_M(\theta^{t+\Delta t} - M_s) - a_{\sigma m}\sigma_m^t - a_{\sigma e}\sigma_{eff}^t]\} \quad (33)$$

where  $a_{\sigma m}$  and  $a_{\sigma e}$  are material parameters for the martensitic transformation which demand experimental evaluation,  $\sigma_m$  and  $\sigma_{eff}$  are the mean and effective stresses at previous time step. For the sake of simplicity,  $a_{\sigma m}$  and  $a_{\sigma e}$  can be assumed as zero.

#### Displacement Field Formulation

Following the same arguments used in the thermal field, for an arbitrary displacement field  $\vec{u}$ , the mechanical equilibrium condition Eq 11 has to satisfy the following integral equation

$$\int_{\Omega} [\nabla \cdot \mathbf{T} + \vec{b}] \cdot \vec{u} d\Omega = 0 \quad (34)$$

Using Gauss divergence theorem, the natural mechanical boundary condition Eq 13 can be substituted in Eq 34, and results in

$$\int_{\Omega} [\mathbf{T} : \vec{\mathbf{E}}] d\Omega = \int_{\Gamma_t} [\vec{t} \cdot \vec{u}] d\Gamma_t + \int_{\Omega} [\vec{b} \cdot \vec{u}] d\Omega \quad (35)$$

The  $x$ ,  $y$  and  $z$  components of the element nodal displacements are given as

$$u_e = \mathbf{N}^T \mathbf{U}_e, \quad v_e = \mathbf{N}^T \mathbf{V}_e, \quad w_e = \mathbf{N}^T \mathbf{W}_e \quad (36)$$

where  $\mathbf{N}$  is the element shape function. The element strains are

$$\mathbf{E}_e = \left[ \left( \frac{\partial u_e}{\partial x} \right) \left( \frac{\partial v_e}{\partial y} \right) \left( \frac{\partial w_e}{\partial z} \right) \left( \frac{\partial u_e}{\partial y} + \frac{\partial v_e}{\partial x} \right) \left( \frac{\partial u_e}{\partial z} + \frac{\partial w_e}{\partial x} \right) \left( \frac{\partial v_e}{\partial z} + \frac{\partial w_e}{\partial y} \right) \right] = \mathbf{B} \hat{\mathbf{U}}_e \quad (37)$$

where  $\mathbf{B}$  is the strain-displacement matrix which is unique for the particular structural problem which will be discussed in the next Section. If  $\omega$  is the number of nodes per element in the mechanical problem, the total elemental displacement degree of freedom vector ( $\hat{\mathbf{U}}_e$ ) is expressed by

$$\hat{\mathbf{U}}_e = \{U_{e1} \quad V_{e1} \quad W_{e1} \quad \dots \quad U_{e\omega} \quad V_{e\omega} \quad W_{e\omega}\}^T \quad (38)$$

where  $\mathbf{U}_e$ ,  $\mathbf{V}_e$ , and  $\mathbf{W}_e$  are the individual  $x$ ,  $y$  and  $z$  directional displacement vectors. Substituting Eqs 36 and 37 into Eq 35,  $\hat{\mathbf{U}}_e$  can be eliminated from both sides. The following incremental relations for every time step with current iteration ( $i+1$ ) are used:

$$\begin{aligned} \Delta \mathbf{E}_e &= \mathbf{B}^T \Delta \hat{\mathbf{U}}_e \\ \Delta \mathbf{T}_e &= \mathbf{C}_{i+1}^{ep, t+\Delta t} \Delta \mathbf{E}_e \\ \hat{\mathbf{U}}_{e, i+1}^{t+\Delta t} &= \hat{\mathbf{U}}_{e_i}^{t+\Delta t} + \Delta \hat{\mathbf{U}}_e \\ \Delta \mathbf{T}_{e, i+1}^{t+\Delta t} &= \Delta \mathbf{T}_{e_i}^{t+\Delta t} + \mathbf{C}_i^{ep, t+\Delta t} \Delta \mathbf{E}_e \end{aligned} \quad (39)$$

where  $\mathbf{C}^{ep}$  is the elemental tangent elasto-plastic matrix [22]. At the beginning of the current time step

$$\begin{aligned} \mathbf{E}_{e_1}^{t+\Delta t} &= \mathbf{E}_e^t + \Delta \mathbf{E}_e^{tp} + \Delta \mathbf{E}_e^{trip} \\ \mathbf{T}_{e_1}^{t+\Delta t} &= \mathbf{T}_e^t \end{aligned} \quad (40)$$

the final global form of mechanical equilibrium equation becomes



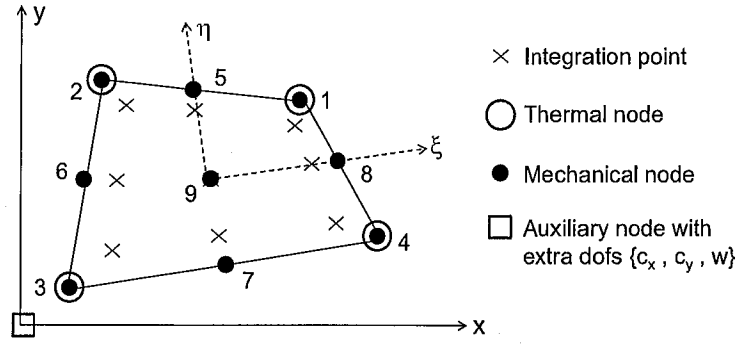


FIG. 1—Layout of a typical element.

$$\mathbf{K}_i^{u^{t+\Delta t}} \Delta \hat{\mathbf{U}} = \mathbf{F}_i^{u^{t+\Delta t}} - \mathbf{R}_i^{u^{t+\Delta t}} \quad (41)$$

where  $\mathbf{K}^u$  is the global stiffness matrix,  $\mathbf{F}^u$  is the global equivalent nodal load vector and  $\mathbf{R}^u$  is the internal reaction vector taken from the previous iteration. Elemental form of matrices and vectors are given as in Ref [27]

$$\begin{aligned} \mathbf{K}_{e_i}^{u^{t+\Delta t}} &= \int_{\Omega} [\mathbf{B}^T \mathbf{C}_i^{ep^{t+\Delta t}} \mathbf{B}] d\Omega \\ \mathbf{F}_e^{u^{t+\Delta t}} &= \int_{\Gamma_f} [(\mathbf{N}^S)^T \mathbf{t}_e^{t+\Delta t}] d\Gamma_f + \int_{\Omega} [\mathbf{N}^T \mathbf{b}_e^{t+\Delta t}] d\Omega \\ \mathbf{R}_{e_i}^{u^{t+\Delta t}} &= \int_{\Omega} [\mathbf{B}^T \mathbf{T}_{e_i}^{t+\Delta t}] d\Omega \end{aligned} \quad (42)$$

where  $\mathbf{t}_e$  is the boundary element traction vector, and  $\mathbf{b}_e$  is the element body force vector.

### Structural Applications

Thermal, metallurgical, and mechanical field computations which are discussed in previous sections are similar for any kind of a three-dimensional metal quenching process except the calculation of strain-displacement matrix  $\mathbf{B}$ . The evaluation of  $\mathbf{B}$  for a particular structure considered are discussed in this section. In this work, two-dimensional structural problems of the following four different cases are studied:

1. plane stress problem
2. plane strain problem
3. axisymmetric problem
4. beam problem

The total strain is the derivative of the displacement field. Therefore, a linear total strain field is obtained for the nine-noded element. In order to have a linear stress field, the thermal strains must also be linear. Since the thermal strains are linear functions of temperature, the thermal field must also be linear. Such a linear thermal field can be provided by four-noded elements. The typical element layout is indicated in Fig. 1.

Using an isoparametric element formulation, the global coordinates and displacements are given in terms of local coordinates  $(\xi, \eta)$  by

$$\left. \begin{aligned} x(\xi, \eta) &= \mathbf{N}^T \mathbf{X} \\ y(\xi, \eta) &= \mathbf{N}^T \mathbf{Y} \end{aligned} \right\} \text{ and } \left. \begin{aligned} u(\xi, \eta) &= \mathbf{N}^T \mathbf{U}_e \\ v(\xi, \eta) &= \mathbf{N}^T \mathbf{V}_e \end{aligned} \right\} \quad (43)$$

The derivatives of shape functions with respect to the global  $x$  and  $y$  coordinates are represented by the operator  $\mathbf{H}$  of size  $2 \times 9$  as

$$\mathbf{H} = \begin{Bmatrix} \frac{\partial}{\partial x} \\ \frac{\partial}{\partial y} \end{Bmatrix} \mathbf{N}^T = \mathbf{J}^{-T} \begin{Bmatrix} \frac{\partial}{\partial \xi} \\ \frac{\partial}{\partial \eta} \end{Bmatrix} \mathbf{N}^T \quad (44)$$

The strain-displacement operator  $\mathbf{B}$  (subscript "e" is suppressed) for the plane stress case is the simplest one and it is referred in this text as standard strain-displacement operator with size  $3 \times 18$ ,

$$\mathbf{B} = \mathbf{B}_{std} = \begin{bmatrix} H_{x1} & 0 & \cdots & H_{x\omega} & 0 \\ 0 & H_{y1} & \cdots & 0 & H_{y\omega} \\ H_{y1} & H_{x1} & \cdots & H_{y\omega} & H_{x\omega} \end{bmatrix} \quad (45)$$

where  $H_x$  and  $H_y$  are the elements of the first and second rows of derivative operator  $\mathbf{H}$ .

The strain-displacement operator for the axisymmetric case has an additional row. Therefore, its size is  $4 \times 18$

$$\mathbf{B} = \begin{bmatrix} \mathbf{B}_{std} \\ \mathbf{B}_{axs} \end{bmatrix}, \quad \text{where } \mathbf{B}_{axs} = \begin{bmatrix} \frac{N_1}{x} & 0 & \cdots & \frac{N_\omega}{x} & 0 \end{bmatrix} \quad (46)$$

where  $x$  is the global radial coordinate.

In this work, a new beam cross-sectional element is introduced to analyze the long profiles which has one extra global node with three degrees of freedom as shown in Fig. 1. The strain-displacement matrix for the beam [5] case has the size  $4 \times 21$ . There is one additional row and three additional columns. The introduced addition is named as  $\mathbf{B}_{beam}$  and

$$\mathbf{B} = \begin{bmatrix} \mathbf{B}_{std} & 0 \\ 0 & \mathbf{B}_{beam} \end{bmatrix}, \quad \text{where } \mathbf{B}_{beam} = \frac{1}{\ell} \begin{bmatrix} 1 & y & -x \end{bmatrix} \quad (47)$$

The additional operator  $\mathbf{B}_{beam}$  is only for computing the strain in the axial direction, which is just related to axial elongation  $w$  and bending curvatures  $c_x$  and  $c_y$ , and  $\ell$  is considered as unity. The standard elasto-plastic stress-strain operator is given as

$$\hat{\mathbf{C}}_{std}^{ep} = 3\kappa \hat{\mathbf{P}}_1 + 2\mu \hat{\mathbf{P}}_2 - \frac{2\mu}{1 + \frac{H}{3\mu}} \hat{\mathbf{n}}'_T - \lambda \frac{4\mu^2}{\|(\mathbf{T}')^{trial}\|} (\hat{\mathbf{P}}_2 - \hat{\mathbf{n}}'_T) \quad (48)$$

where  $\hat{\mathbf{P}}_1$  is the spherical projector,  $\hat{\mathbf{P}}_2$  is the deviator projector, and  $\hat{\mathbf{n}}'_T$  is the plastic flow direction projector. Since in the case of plane stress case the stress in the perpendicular direction is zero, the projectors are of size  $3 \times 3$

$$\hat{\mathbf{P}}_1 = \frac{1}{3} \begin{bmatrix} 1 & 1 & 0 \\ 1 & 1 & 0 \\ 0 & 0 & 0 \end{bmatrix}, \quad \hat{\mathbf{P}}_2 = \frac{1}{2} \begin{bmatrix} +\frac{4}{3} & -\frac{2}{3} & 0 \\ -\frac{2}{3} & +\frac{4}{3} & 0 \\ 0 & 0 & 1 \end{bmatrix}, \quad \hat{\mathbf{n}}'_T = \mathbf{n}'_T (\mathbf{n}'_T)^T = \frac{\mathbf{T}' (\mathbf{T}')^T}{\|\mathbf{T}'\|^2} \quad (49)$$

For all other cases (plane strain, axisymmetric, and beam cases), the projectors are of size  $4 \times 4$

$$\hat{\mathbf{P}}_1 = \frac{1}{3} \begin{bmatrix} 1 & 1 & 0 & 1 \\ 1 & 1 & 0 & 1 \\ 0 & 0 & 0 & 0 \\ 1 & 1 & 0 & 1 \end{bmatrix}, \quad \hat{\mathbf{P}}_2 = \frac{1}{2} \begin{bmatrix} +\frac{4}{3} & -\frac{2}{3} & 0 & -\frac{2}{3} \\ -\frac{2}{3} & +\frac{4}{3} & 0 & -\frac{2}{3} \\ 0 & 0 & 1 & 0 \\ -\frac{2}{3} & -\frac{2}{3} & 0 & +\frac{4}{3} \end{bmatrix} \quad (50)$$

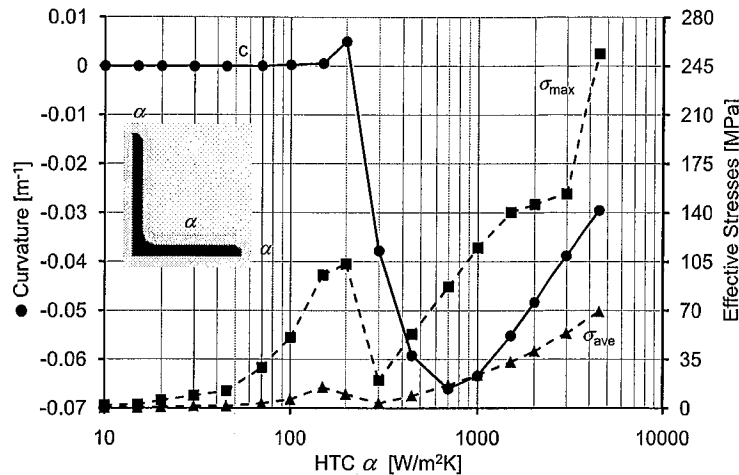


FIG. 2—HTC  $\alpha$  versus curvature and effective stresses in equal cooling of L-100Cr6.

## Results and Discussions

The developed thermo-mechano-metallurgical model is applied to the quenching simulation of beams having L and T cross sections and disk with a circular hole made up of 100Cr6 steel and aluminum. The temperature-dependent material properties of the individual phases can be found in Ref [3]. The distortion of the long profiles is represented by its curvature. The distortion of the circular disk with a hole is described by the standard deviation of its radial displacement. A modification of the local cooling to reduce the distortion and residual stresses has been introduced. The volume averages of the temperature and the effective stresses are considered for the comparison of different cooling strategies. The cooling profile optimization technique is introduced and presented in detail. Finally, the equal and optimum cooling strategies are compared and results are presented in this section.

### L-Profile

**Equal Cooling**—An L120 × 12 profile made up of 100Cr6 steel of unit length is modeled using the *beam cross-sectional elements* as discussed in the Structural Applications section. A series of simulations with equal HTC ( $\alpha$ ) ranging from 10–4500 W/m<sup>2</sup> K has been performed to find out the critical cooling regions. The computed final distortion, the average and the maximum effective stresses are plotted against  $\alpha$  in Fig. 2. In the low cooling range  $\alpha < 200$  W/m<sup>2</sup> K no distortion is observed and it increases in the negative direction, reaches maximum at  $\alpha = 700$  W/m<sup>2</sup> K and then changes its direction. The internal stresses gradually increase with the increasing  $\alpha$  in the low cooling range and reaches to a local maximum where the distortion of the profile is first observed. Next, a local minimum of stress indicates that the different parts of the profile are plastified in the reverse directions which produce the distortion but at the same time relaxes the residual stress state. The cooling behavior of the profile is highly depends on the material properties as well as local HTCs [5].

**Enhanced and Reduced Cooling**—The heat in the body flows to the surrounding through its boundary. During an equal quenching process, the temperature gradient is not uniform due to mass distribution with respect to the locations of the boundaries. It has been already proved in Ref [3] that the distortion can be eliminated by increasing the local cooling at mass lumped regions. This fact is verified in this section with the first cooling strategy as shown in Fig. 3. Increasing the HTC only at the mass lumped region moderately equalizes the temperature distribution. The HTC at the mass lumped region is designated by  $\alpha_1$ . As the HTC  $\alpha_1$  is increased, the distortion gets reduced and totally eliminated at  $\alpha_1 = 1315$  W/m<sup>2</sup> K. Further increase in the HTC  $\alpha_1$  produces a distortion in the reverse direction. However, this strategy increases the residual stress continuously as shown in Fig. 3. From this simulation result, one can come to the conclusion that increasing the HTC at the mass lumped region can only reduce the distortion but not the residual stresses.

As a consequence, a better strategy is required which minimizes the distortion and the stresses simul-

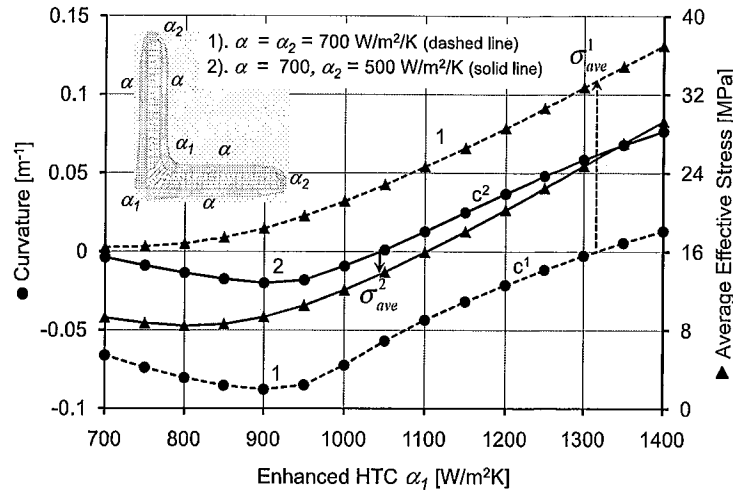


FIG. 3—Curvature and average effective stress as a function of enhanced HTC  $\alpha_1$  (L-100Cr6).

taneously. Secondly, reducing the cooling at the edges and enhancing the cooling at mass lumped region equalize the temperature distribution inside the material to a greater extent [4]. To implement this, Strategy 2 in which  $\alpha_2 = 500 \text{ W/m}^2 \text{ K}$  is maintained at the edges along with uniform cooling of  $\alpha = 700 \text{ W/m}^2 \text{ K}$ , the curvature and the stress are plotted for various values of the enhanced cooling HTC  $\alpha_1$ . The distortion is completely eliminated when  $\alpha_1$  reaches  $1040 \text{ W/m}^2 \text{ K}$ . The residual stress at zero curvature in Strategy 2 is half the value of Strategy 1. This fact indicates that by an optimal combination of  $\alpha_1$  and  $\alpha_2$ , there is a possibility of obtaining least distortion with minimum residual stress.

**Optimum Cooling**—The equal cooling study gives an idea about the cooling range at which maximum distortion occurs. An enhanced cooling at the mass lumped region along with a uniform cooling eliminates the distortion at the expense of increased residual stresses. Simultaneous enhanced and reduced cooling based on the mass concentration brings both the distortion and residual stresses to a lower value. In search of an optimum value of enhanced  $\alpha_1$  and reduced  $\alpha_2$  HTC for a particular value of the uniform HTC  $\alpha$  is obtained with the help of following procedures:

1. Identify the mass lumped regions, edges, and corners in the structure. For a complex structure, the temperature distribution after some time of an equal cooling gives an idea of the mass concentrations. The mass lumped regions are indicated by the hot zones and the low mass regions like edges are indicated by the cooler regions. The HTC assigned to the mass lumped regions is called as  $\alpha_1$  and the low mass regions as  $\alpha_2$ . Except those two regions, the uniform HTC of  $\alpha$  is assigned throughout the structure.
2. The curvature  $c$  can be considered as a measure of distortion of the long profiles. The average effective stress  $\sigma_{ave}$  can be treated as a measure of residual stress. The objective of this optimization is to reduce the distortion and residual stresses simultaneously. Therefore, the curvature is multiplied by the factor  $\psi$  and added to the stress. The optimization problem is defined as

$$\text{argmin}_{\alpha_1 \in [\alpha, \alpha_u], \alpha_2 \in [\alpha_l, \alpha]} \{Z(\alpha_1, \alpha_2) = \sigma_{ave} + \psi|c|\} \quad (51)$$

where  $\sigma_{ave}$  is substituted in terms of MPa,  $\alpha_l \approx 0.1\alpha$  is the lower bound, and  $\alpha_u \approx 2\alpha$  is the upper bound. For the L profile,  $\psi$  is taken as  $1 \times 10^5$ . The objective function  $Z$  has to be minimized for the decision variables  $\alpha_1$  and  $\alpha_2$ .

Finding the solution for this optimization problem is difficult due to the following reasons: (a) stress and curvature are very complex function of the decision variables which involves the solution of the coupled nonlinear partial differential equations, (b) during the optimization, one has to run the entire quenching simulation for every single combination of  $\alpha_1$  and  $\alpha_2$ , which consumes a lot of computational time.

For  $\alpha = 700 \text{ W/m}^2 \text{ K}$ , the objective function is estimated for various values of  $\alpha_1$  and  $\alpha_2$  and plotted in a contour map. The resolution of the plot can be increased by using a cubic interpolation to generate more data points which will help to locate the minimum regions as shown in Fig. 4. From Fig. 4, it is easier to

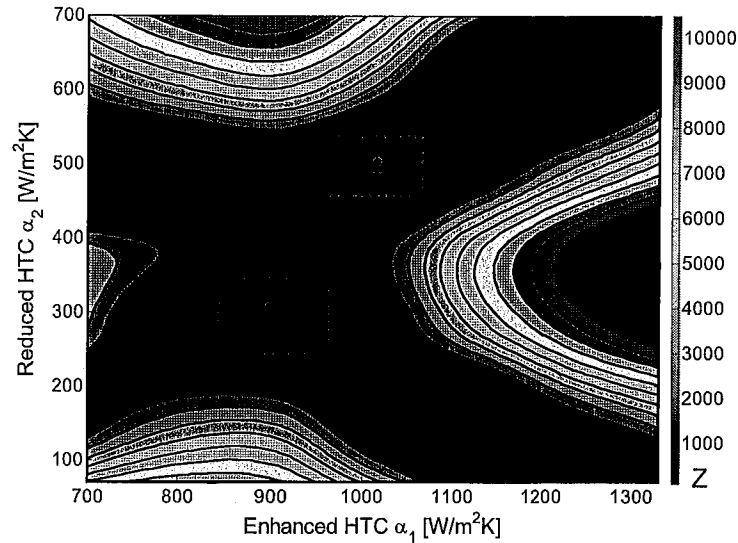


FIG. 4—Contour plot of objective function  $Z$  as a function of  $\alpha_1$  and  $\alpha_2$  (L-100Cr6).

locate the region at which  $Z$  attains minimum value. The contour inside the dotted rectangles in Fig. 4 represent the possible regions at which  $Z$  reaches minimum. Within this bounded region, the optimum value of  $\alpha_1$  and  $\alpha_2$  can be obtained through the trial and error method.

The evolution of the average temperature and the maximum temperature difference for the equal cooling and one of the optimum cooling is plotted in Fig. 5. It is obvious that the average temperature evolutions are almost the same for both types of cooling, but the maximum temperature difference is lower in the case of optimum cooling which indicates that the optimum cooling provides a more uniform distribution. The lower temperature difference provides less thermal stresses. In addition, it provides a more uniform phase transition with less transformation stresses. Similar to the average temperature evolution, the martensite and pearlite phase evolutions are also almost the same as shown in Fig. 6. That means the equal and optimized cooling results in a very similar micro-structure with much less distortion and residual stresses as shown in Figs. 7 and 8, respectively.

In the case of an optimum cooling strategy, the distortion is much smaller during the cooling, and it is finally eliminated as shown in Fig. 7. The evolutions of the average and maximum effective stresses for the equal cooling and optimum cooling are plotted in Fig. 8. The final maximum effective stress is reduced approximately from 87.2 MPa to 24 MPa. Similarly, the average effective stress is reduced from 16.4 MPa to 10.1 MPa. During the phase transformation the maximum effective stress fluctuates a lot due to the transformation induced plasticity.

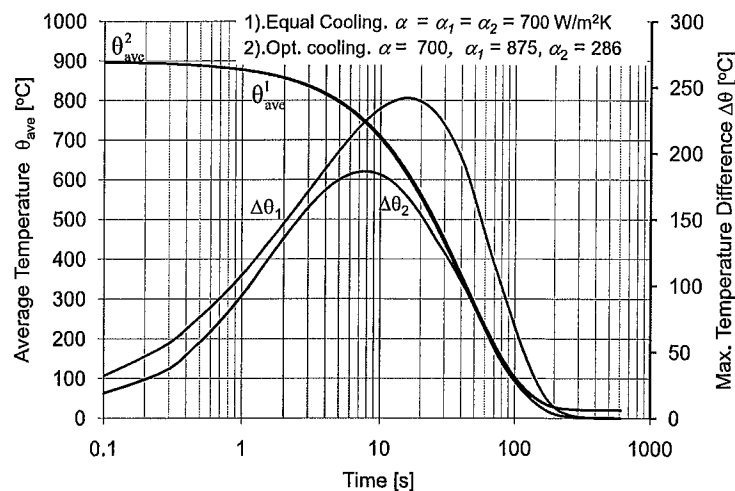


FIG. 5—Comparisons: Equal and optimum cooling strategies—temperature evolution.

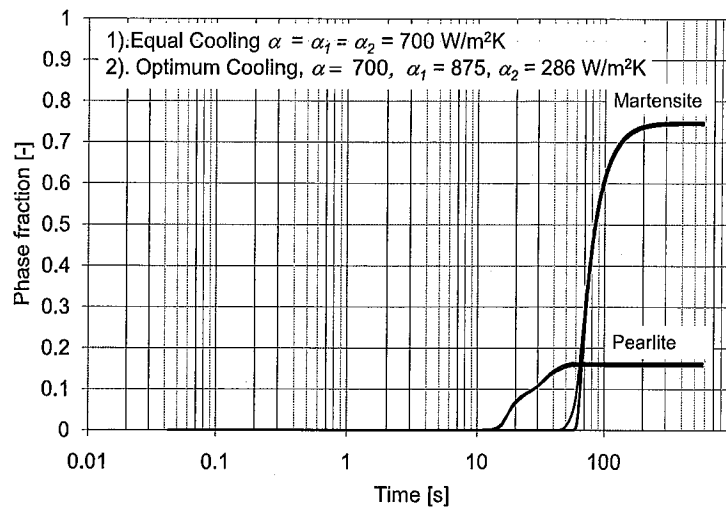


FIG. 6—Comparisons: Equal and optimum cooling strategies—phase evolution.

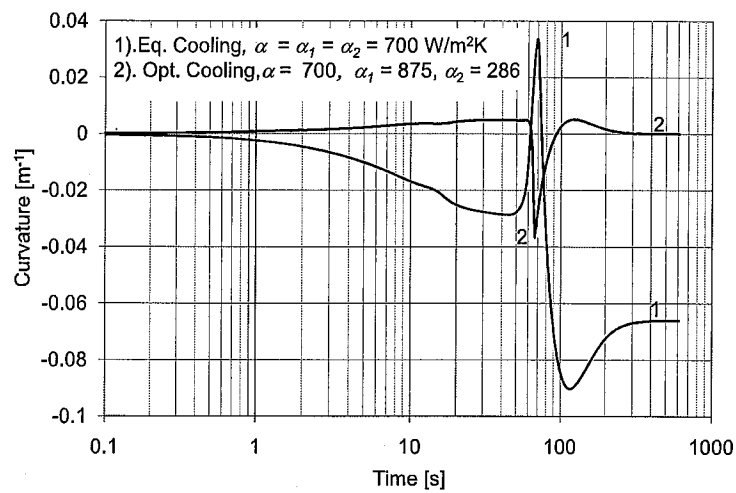


FIG. 7—Comparisons: Equal and optimum cooling strategies—curvature evolution.

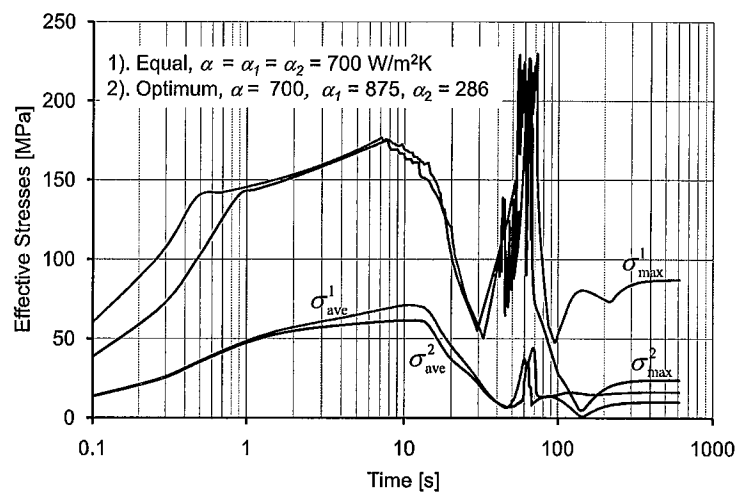


FIG. 8—Comparisons: Equal and optimum cooling strategies—effective stresses evolution.

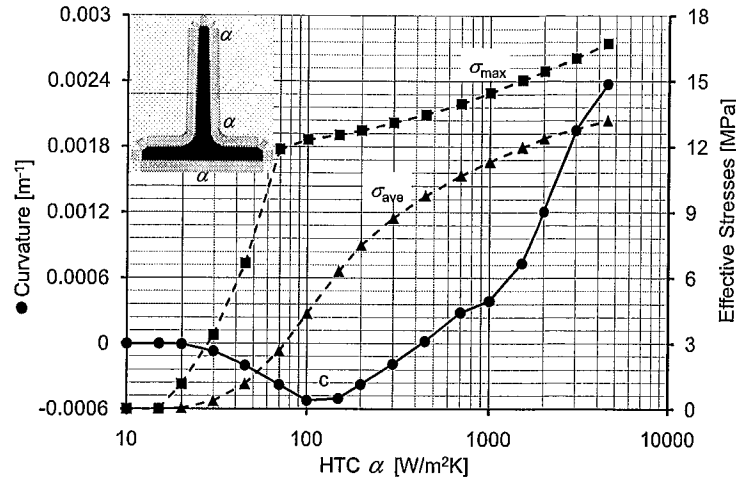


FIG. 9—Curvature and effective stresses versus equal cooling HTC  $\alpha$  (T-Aluminum).

#### T—Profile

A T120  $\times$  12 profile made of aluminum, is modeled using the *beam cross-sectional elements*, similar to the L profile, for the understanding of nonphase changing material behavior during the quenching process. To identify the region of equal cooling at which maximum distortion and residual stress occur, equal cooling simulation results are presented in Fig. 9. The distortion direction changes during the cooling when the HTC  $\alpha = 100$  W/m<sup>2</sup> K. Unlike steel, the maximum distortion and stresses occur at most intensive cooling.

Using the similar arguments as in the L profile, the optimum cooling strategy is identified for the T-Aluminum profile at  $\alpha = 4500$  W/m<sup>2</sup> K. Through the optimum strategy, a significant reduction in average and maximum effective stresses are achieved when compared to equal cooling strategy, and distortion gets completely eliminated as shown in Fig. 10. Not only the final distortion, but also the evolution of distortion itself gets reduced which is highly favorable for avoiding high plastic deformation.

#### Disk with a Hole

A thin circular 100Cr6 steel disk, having a sharp outer edge with a central hole and one-quarter of the outer edge straightly truncated is considered as shown in Fig. 11. Quenching of the thin disk is modeled using the *plane stress elements* with additional volumetric force vector. The distortion of the disk is described by the deviation of the central hole from the perfect circle. The area of the outer sharp edge is approximately one-half of the surface area of the circular hole. The distortion of the central hole during quenching is

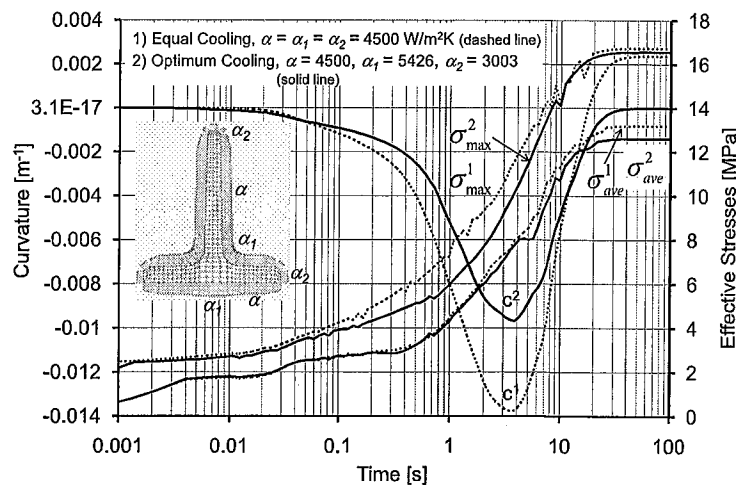


FIG. 10—Comparisons: Equal and optimum cooling strategies—curvature and effective stresses evolution (T-Aluminum).

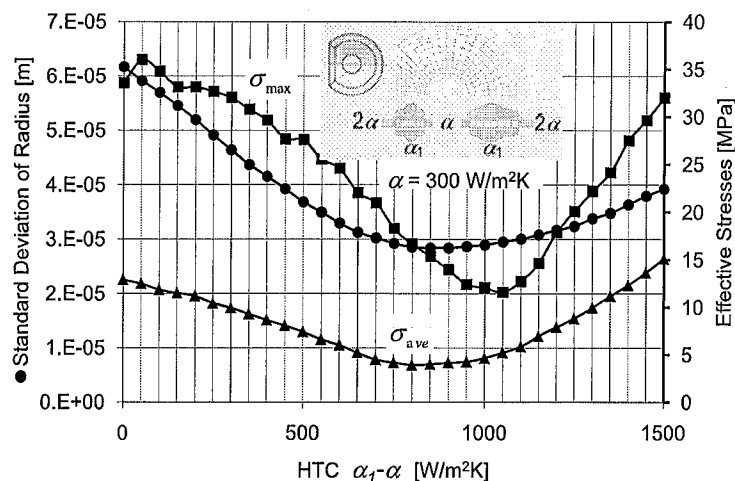


FIG. 11—Disk with a hole: Relative enhanced HTC versus distortion and effective stresses.

experimentally verified in the previous work [2] of the authors for equal cooling. In this case, there is no specific mass lumped region but due to the limited conductivity, the central portion of the annular region is always hotter than the other regions. The enhanced HTC at the center of the annular region is designated by  $\alpha_1$ . The sharp edges are not relatively colder during equal cooling because for compensating the surface heat flux at the sharp edge, double the value of equal HTC  $\alpha$  is assigned.

Due to the absence of  $\alpha_2$ , the objective function of the optimization technique discussed in the beam case is simplified into one parameter ( $\alpha_1$ ) optimization. For various values of relative enhanced HTCs ( $\alpha_1 - \alpha$ ), the distortion and effective stresses are plotted in Fig. 11. Both the distortion and average effective stresses reach minimum at  $\alpha_1 - \alpha = 850 \text{ W/m}^2 \text{ K}$  and maximum effective stresses attains the least value at  $\alpha_1 - \alpha = 1050 \text{ W/m}^2 \text{ K}$  as shown in Fig. 11.

Three different cooling strategies of relative HTCs  $\alpha - \alpha_1 = 0, 1050$  and  $850 \text{ W/m}^2 \text{ K}$ , with  $\alpha_1 = 300 \text{ W/m}^2 \text{ K}$  are analyzed. Effective stresses evolution and distortion evolutions are compared as shown in Figs. 12 and 13, respectively.  $\alpha - \alpha_1 = 0 \text{ W/m}^2 \text{ K}$  represents the equal cooling which produces higher stresses and distortion. Within the another two strategies, third strategy  $\alpha - \alpha_1 = 850 \text{ W/m}^2 \text{ K}$  minimizes the distortion and average effective stress, therefore this strategy can be considered as an optimum cooling strategy for the disk with a hole at  $\alpha = 300 \text{ W/m}^2 \text{ K}$ .

### Concluding Remarks

The metal quenching process is simulated using a nonlinear finite element technique which includes the coupling of thermal, metallurgical, and mechanical fields within the frame of the isothermal staggered

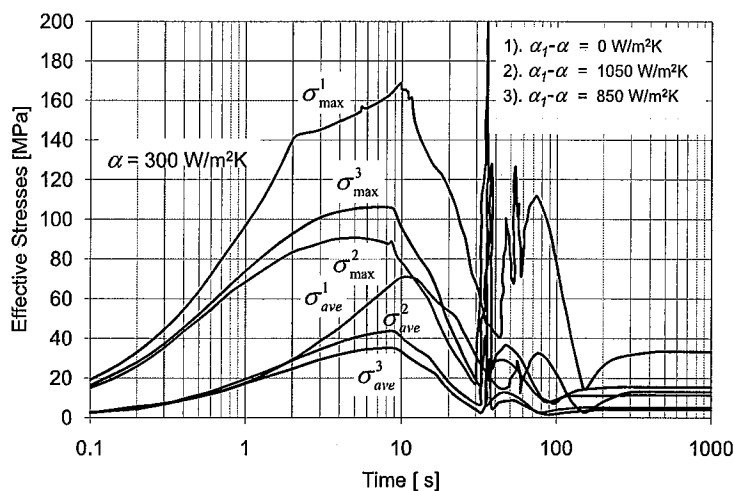


FIG. 12—Disk with a hole: comparison of cooling strategies—stress evolution.



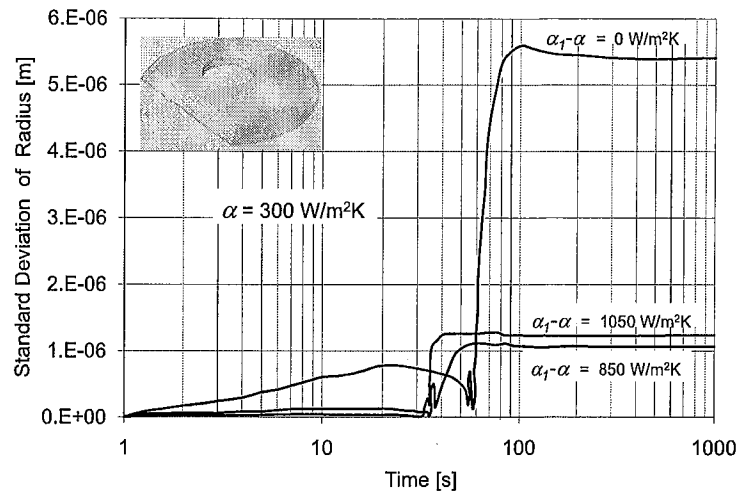


FIG. 13—Disk with a hole: comparison of cooling strategies—distortion evolution.

approach. The distortion and residual stresses evolution are calculated for long **L** and **T** profiles made of 100Cr6 steel and aluminum using a newly introduced beam cross-sectional element. The heat transfer coefficient (HTC) plays a major role for the temperature distribution inside the material, and it affects the final distortion and residual stresses. Equal cooling does not equalize the temperature distribution. The distortion can be eliminated with the help of enhanced cooling at the mass lumped region but it increases the residual stresses. Along with an enhanced cooling at mass lumped region, a reduced cooling at the edges and corners simultaneously reduces both the distortion and residual stresses. Using this methodology, enhanced and reduced HTC's are optimized and stresses and distortion are brought in to the least possible value. Equal cooling and optimum cooling strategies are compared, and the necessity of optimum quenching strategy is proved using volume averaged stress and temperature plots. A disk with a hole is also studied using plane stress element and the deviation of central hole radius is compared for equal and optimum cooling.

#### Acknowledgments

The financial support provided by German Science Foundation (DFG) through GKMM graduate school, Magdeburg, Germany, is greatly acknowledged.

#### References

- [1] Pietzsch, R., Brzoza, M., Kaymak, Y., Specht, E., and Bertram, A., "Minimizing the Distortion of Steel Profiles by Controlled Cooling," *Asian J. Chem.*, Vol. 76, 2005, pp. 399–407.
- [2] Brzoza, M., Specht, E., Ohland, J., Belkessam, O., Lübken, T., and Fritsching, U., "Minimizing Stress and Distortion for Shafts and Discs by Controlled Quenching in a Field of Nozzels," *Mat. Sci. Engg. Tech.*, Vol. 37, 2006, pp. 97–102.
- [3] Pietzsch, R., Brzoza, M., Kaymak, Y., Specht, E., and Bertram, A., "Simulation of the Distortion of Long Steel Profiles During Cooling," *J. Appl. Mech.*, Vol. 74, 2007, pp. 427–437.
- [4] Kaymak, Y. and Specht, E., "Strategies for Controlled Quenching to Reduce Stresses and Distortion," *Heat Proc.*, Vol. 5, No. 3, 2007, pp. 1–4.
- [5] Kaymak, Y., "Modeling of Metal Quenching Process and Strategies to Minimize Distortion and Stresses," Ph.D. thesis, Otto-von-Guericke University, Magdeburg, Germany, <http://diglib.uni-magdeburg.de/Dissertationen/2007/yalkaymak.pdf>
- [6] Lewis, R. W. and Ravindran, K., "Finite Element Simulation of Metal Casting," *Int. J. Numer. Methods Eng.*, Vol. 47, 2000, pp. 29–59.

- [7] Çetinel, H., Toparli, M., and Özsoyeller, L., "A Finite Element Based Prediction of the Microstructural Evolution of Steels Subjected to the Tempcore Process," *Mech. Mater.*, Vol. 32, No. 6, 2000, pp. 339–347.
- [8] Reti, T., Fried, Z., and Felde, I., "Computer Simulation of Steel Quenching Process Using a Multi-Phase Transformation Model," *Comput. Mater. Sci.*, Vol. 22, No. 3–4, 2001, pp. 261–278.
- [9] Kang, S. H., and Im, Y. T., "Finite Element Investigation of Multi-Phase Transformation Within Carburized Carbon Steel," *J. Mater. Process. Technol.*, Vol. 183, 2007, pp. 241–248.
- [10] Facinotti, V. D., Cardona, A., and Anca, A. A., "Solid State Microstructure Evolution in Steels," *Mecanica Comp.*, Vol. XXIV, 2005, pp. 901–914.
- [11] Prantil, V. C., Callabresi, M. L., Lathrop, J. F., Ramaswamy, G. S., and Lusk, M. T., "Simulating Distortion and Residual Stresses in Carburized Thin Strips," *J. Eng. Mater. Technol.*, Vol. 125, 2003, pp. 116–124.
- [12] Huiping, L., Guoqun, Z., Shanting, N., and Yiguo, L., "Technologic Parameter Optimization of Gas Quenching Process Using Response Surface Method," *Comput. Mater. Sci.*, Vol. 38, 2007, pp. 561–570.
- [13] Liu, C., Ju, D. Y., and Inoue, T., "A Numerical Modeling of Metallo-Thermo-Mechanical Behavior in Both Carburized and Carbonitrided Quenching Processes," *ISIJ Int.*, Vol. 42, No. 10, 2002, pp. 1125–1134.
- [14] Liu, C. C., Xu, X. J., and Liu, Z., "A FEM Modeling of Quenching and Tempering and Its Application in Industrial Engineering," *Finite Elem. Anal. Design*, Vol. 39, 2003, pp. 1053–1070.
- [15] Li, Z., Grandhi, R. V., and Srinivasan, R., "Distortion Minimization During Gas Quenching Process," *J. Mater. Process. Technol.*, Vol. 172, 2006, pp. 249–257.
- [16] Ju, D. Y., Zhang, W. M., and Zhang, Y., "Modeling and Experimental Verification of Martensitic Transformation Plastic Behavior in Carbon Steel for Quenching Process," *Mater. Sci. Eng., A*, Vol. 438–440, 2006, pp. 246–250.
- [17] Hamouda, A. M. S., and Sulaiman, S., "Finite Element Analysis on the Effect of Work Piece Geometry on the Quenching of the ST50 Steel," *J. Mater. Process. Technol.*, Vol. 119, 2001, pp. 354–360.
- [18] Koc, M., Culp, J., and Altan, T., "Prediction of Residual Stresses in Quenched Aluminum Blocks and Their Reduction Through Cold Working Processes," *J. Mater. Process. Technol.*, Vol. 174, 2006, pp. 342–354.
- [19] Hossain, S., Daymond, M. R., Truman, C. E., and Smith, D. J., "Prediction and Measurement of Residual Stresses in Quenched Stainless-Steel Spheres," *Mater. Sci. Eng., A*, Vol. 373, 2004, pp. 339–349.
- [20] Newman, M. L., Robinson, B. J., Sehitoglu, H., and Dantzig, J. A., "Deformation, Residual Stress, and Constitutive Relations for Quenched W319 Aluminum," *Metall. Mater. Trans. A*, Vol. 34A, 2003, pp. 1483–1491.
- [21] Celentano, D., Orate, E., and Oller, S., "A Temperature-Based Formulation for Finite Element Analysis of Generalized Phase-Change Problems," *Int. J. Numer. Methods Eng.*, Vol. 37, 1994, pp. 3441–3465.
- [22] Simo, J. C., and Hughes, T. J. R., *Computational Inelasticity*, Springer Verlag, New York, 1997.
- [23] Greenwood, G. W., and Johnson, R. H., "The Deformation of Metals Under Small Stress During Phase Transformation," *Proc. R. Soc. London, Ser. A*, Vol. A283, 1965, pp. 403–422.
- [24] Chen, W. F., *Constitutive Equations for Engineering Materials, Vol.2 Plasticity and Modelling*, Elsevier, Amsterdam, 1994.
- [25] Armero, F. and Simo, J. C., "A New Unconditionally Stable Fractional Step Method for Nonlinear Coupled Thermomechanical Problems," *Int. J. Numer. Methods Eng.*, Vol. 35, 1992, pp. 737–766.
- [26] Agelet deSaracibar, C., Cervera, M., and Chiumenti, M., "On the Formulation of Coupled Thermo-plastic Problems with Phase-Change," *Int. J. Plast.*, Vol. 15, 1999, pp. 1–34.
- [27] Bathe, K. J., *Finite Element Procedures in Engineering Analysis*, Prentice-Hall, New Jersey, 1982.